Proteomics reveals long-term alterations in signaling and metabolic pathways following both myocardial infarction and chemically induced denervation

Jennifer Ben Salem, Jason Iacovoni, Denis Calise, D. N. Arvanitis, Francis Beaudry

nProteomics reveals long-term alterations in signaling and metabolic pathways following both myocardial infarction and chemically induced denervation

Jennifer Ben Salem[1,2,3,a], Jason S Iacovoni[1,a], Denis Calise[4], Dina N Arvanitis[1*], Francis Beaudry[2,3*]

1-INSERM DR Midi-Pyrénées Limousin, Institut des Maladies Métaboliques et Cardiovasculaires (I2MC) UMR1297, Université de Toulouse III, France
2- Département de Biomédecine Vétérinaire, Faculté de Médecine Vétérinaire, Université de Montréal, Saint-Hyacinthe, Québec, Canada
3-Centre de recherche sur le cerveau et l'apprentissage (CIRCA), Université de Montréal, Montréal, Québec, Canada
4-INSERM DR Midi-Pyrénées Limousin, Centre Régional d'Exploration Fonctionnelle et Ressources Expérimentales Service Microchirurgie, (CREFRE- US06, Rangueil)

[a] co-first author. These authors contributed equally to this work.

* co-corresponding authors
Francis Beaudry, Ph.D.
Professor of Analytical Pharmacology
Canada Research Chair in metrology of bioactive molecule and target discovery
Département de Biomédecine Vétérinaire
Faculté de Médecine Vétérinaire
Université de Montréal
3200 Sicotte
Saint-Hyacinthe, QC
Canada J2S 2M2
Email: francis.beaudry@umontreal.ca

Dina N. Arvanitis, Ph.D.
Research Scientist CNRS
Institut des Maladies Métaboliques et Cardiovasculaires (I2MC) UMR INSERM 1297 - Équipe 10
1 Avenue Jean Poulhès,
BP 84225
31432 Toulouse Cedex . tel : +33 (0)5224072
Email: constandina.arvanitis@univ-tlse3.fr

Keywords: myocardial infarction, heart failure, resiniferatoxin (RTX), Transient receptor potential vanilloid subtype 1 (TRPV1) (TRPV1), proteomics, mass spectrometry, bioinformatics, integrative biology, autonomic nervous system.

Abstract

Myocardial infraction (MI) is the principal risk factor for the onset of heart failure (HF). Investigations regarding the physiopathology of MI progression to HF have revealed the concerted engagement of other tissues, such as the autonomic nervous system and the medulla oblongata (MO), giving rise to systemic effects, important in the regulation of heart function. Cardiac sympathetic afferent denervation following application of resiniferatoxin (RTX) attenuates cardiac remodelling and restores cardiac function following MI. While the physiological responses are well documented in numerous species, the underlying molecular responses during the initiation and progression from MI to HF remains unclear. We obtained multi-tissue time course proteomics with a murine model of HF induced by MI in conjunction with RTX application. We isolated tissue sections from the left ventricle (LV), MO, cervical spinal cord and cervical vagal nerves at four time points over a 12-week study. Bioinformatic analyses consistently revealed a high statistical enrichment for metabolic pathways in all tissues and treatments, implicating a central role of mitochondria in the tissue-cellular response to both MI and RTX. In fact, the additional functional pathways found to be enriched in these tissues, involving the cytoskeleton, vesicles and signal transduction, could be downstream of responses initiated by mitochondria due to changes in neuronal pulse frequency after a shock such as MI or the modification of such frequency communication from the heart to the brain after RTX application. Development of future experiments, based on our proteomic results, should enable the dissection of more precise mechanisms whereby metabolic changes in neuronal and cardiac tissues can effectively ameliorate the negative physiological effects of MI via RTX application.

Introduction

Heart failure (HF) is a global health burden due to the increased life expectancy of individuals that survive acute myocardial infarction (MI) [1]. MI to HF progression is a complex clinical syndrome believed to be caused by inadequate cardiac output, which is unable to meet systemic metabolic requirements [2–4]. The systemic pathophysiological consequences of HF are particularly important and there has been a growing awareness concerning the link between the heart and brain dysfunction [5, 6]. Over the past few decades, we have started to reveal the the basic pathophysiology underlying the heart–brain axis [7, 8]. While evidence suggested principally the role of adverse drug reactions, cranial hemodynamic changes in MI have gained considerable interest [3, 9, 10]. A recent systematic review suggested cardiac dysfunction hindered cerebral blood flow and may predisposes one to cognitive decline [11], but others suggest it may not be a predominant factor in HF-associated nervous system dysfunction [7, 12].

An important hallmark of HF is the modification in activity of the autonomic nervous system (ANS), with sympathetic nervous system (SNS) hyperactivity largely contributing to disease progression and negative outcome [13–15]. The predominant notion in the field is that HF leads to the hyperactivation of SNS efferent brain-to-heart fibers, thereby amplifying the damage to cardiac muscle [15]. The mechanism of this SNS hyperactivity is only partially known. Proposed mechanisms accounting for increased SNS activity include deactivation of baroreflex feedback and hemodynamic modifications in HF or hyperactivity of chemoreflexes related to anemia, renal failure or cardio-renal syndrome [16–18]. The initial trigger of the SNS as a physiological consequence of HF has also been studied extensively in the clinic [15, 19, 20]. More recently, we and others have shown that SNS hyperactivity is regulated by the denervation of a subset of cardiac afferent fibers expressing the Transient receptor potential vanilloid

subtype 1 (TRPV1), a non-selective cation channel [21]. The desensitization of cardiac afferents by Resiniferatoxin (RTX), an ultrapotent analogue of capsaicin and an agonist of TRPV1, reduces both the sympathetic tone downstream of MI and cardiac infarct size [22–26]. Furthermore, we recently demonstrated that this desensitization relieves the despair phenotype induced by HF in a murine model [27]. These cardiac afferents form a portion of the sympathetic cardiac network initiating in the spinal cord onto ascending pathways into the medulla oblongata (MO) and are traced to the lateral basal frontal cortex [28, 29]. The activity of these spinal afferents is further exemplified by Wu and colleagues [30] who show that central chemo-ablation of the TRPV1+ afferents in the spinal cord prevent ventricular arrhythmias in heart failure via selectively blunting cardiac sympathetic afferent projection into the spinal cord.

HF neural imbalances are not limited to the SNS, traveling via spinal ganglia to the heart, but also to the parasympathetic nervous system (PNS), implicating the thoracic ganglia as well as the right and left vagal trunks [22, 31, 32]. Withdrawal of vagal activity in HF, or reduction in parasympathetic innervation of the heart, occurs at early stages of left ventricular dysfunction and this reduction is associated with worse outcomes in patients following MI with HF [33]. Studies thus far have shown that ameliorating vagal activity improves cardiac function and HF patient outcome [34, 35], however vagal stimulation therapy remains controversial [36]. Neural communication between the heart and brain is highly complex; and apart from neurophysiological assessments following stimulation or suppression, very little is known about the molecular components eliciting the responses. Here we sought to identify the immediate and longer-term molecular components in this neural circuit. The protein communities elicited downstream of MI, and the early dynamics of these responses during the progression to HF were studied by using mass spectrometry-based proteomics. For these analyses, we used an experimental MI and HF animal model (MI group) as previously described [27]. To identify the

contribution of TRPV1 expressing cardiac afferents, RTX was acutely applied to the pericardial space in a subset of mice to monitor its effect in both control (RTX) and in MI treated animals (MI/RTX). Tissues were isolated immediately following MI at 5 min and 20 min. In addition, animals were permitted to awaken, and tissues were collected at 24H and 12-week time points. Samples from the four tissues at these four time points were then processed for mass spectrometry followed by proteomic analyses. Hierarchical clustering and subsequent tree cutting were used to partition proteins based on their expression profile, with respect to sham controls, over time. Clustered proteins were further analysed by functional enrichment analysis using EnrichR [37–39]. We show that despite the large amount of overlap in terms of proteins and functional pathways, each tissue and treatment resulted in distinct change over the time course investigated.

Materials and Methods

Animal Husbandry

Ten-week-old male C57BL/6J mice were purchased from a commercial supplier (Envigo, Gannat, France) and were allowed to habituate to the animal facility for 12-16 days prior to the experiments. Males were chosen to reduce sex-based variability observed in the heart [40, 41] and brain, particularly in mood disorders [42]. Mice were housed in groups of 5 on a 12-h light/dark cycle and an ambient temperature of 22 ± 3 °C, with food and water available ad libitum. Animal procedures were approved by the national Animal Care and Ethics Committee (CE2A122 protocol number 2016101916279704) following Directive 2010/63/EU.

Myocardial Infarction and RTX application

MI was performed as previously described [27]. Briefly, animals received a chemical induction of ketamine / xylazine (125/5 mg/kg) by intraperitoneal injection followed by a gas induction

by 2% of isoflurane inhalant mixed with 1 L/min 100% O2. Tracheal intubation was performed under a binocular microscope. RTX (Tocris Bioscience, Rennes, France) was prepared as previously described [43] and 10 µL of 0.25 µg/mL saline solution was used for pericardial injections. Animals were respirated with mini-wind ventilators (Harvard Apparatus, Les Ulis, France). Surgical procedures were performed under a Zeiss OPM1 FC operating microscope (Zeiss, Paris, France). An incision of the 4th intercostal space was performed to provide adequate exposure of the thoracic cavity. The left atrioventricular block was exposed, an 8/0 Prolene thread (Ethicon) was placed at the edge of the left atrial appendage and a catheter was used to inject 10 µL of saline or RTX saline solution within the intrapericardium just prior to ligature. Evans Blue was used as a tracking dye to ensure lack of spillage. Immediately following infarction, 10 µL of saline (i.e., Sham group) or RTX (i.e., MI/RTX and RTX group) at 0.25 µg/mL was injected. The intercostal space was sutured followed by closing the skin surface using an Ethilon 6/0 thread (Ethicon). For acute MI animals were kept on anaesthesia and respiration for 5 min before tissues were dissected. All other animals received Buprecare (Buprenorphine) subcutaneously (100 µg/kg) as mandated by the National Ethics Board. RTX concentrations (i.e., 0.25 µg/mL) used in our study were based on previous studies [26, 27, 43, 44]. All surgical procedures were performed between 7h-13h.

Tissue dissection and preparation

For the T1 (5 min) and T2 (20 min) time points, the subjects were maintained on isoflurane and artificial respiration for the desired time and then animals were sacrificed, and tissues (left ventricle, medulla oblongata, spinal cord (i.e., C1-C4) and cervical vagal nerves) were isolated. For the T3 (24h) and T4 (12-weeks) time points, mice were anaesthetized with isoflurane, weighed and sacrificed by cutting the spine at the skull base. Tissues were immediately removed and rinsed in dissection buffer; ice-cold PBS supplemented with Protease and Phosphatase

Inhibitors (Merck, France) and 10 nM of Phenylmethanesulfonyl fluoride (PMSF, Merck, France). Microdissection was also performed in ice-cold dissection buffer.

Sample preparation for proteomics

Mouse tissues were weighed and then homogenized using a Bead Mill Homogenizer (Fisherbrand) following the addition of a solution of 8 M urea in 100 mM TRIS-HCL buffer (pH 8) containing a cocktail of protease inhibitors (cOmplete, Sigma-Aldrich, Oakville, ON, Canada) at a ratio of 1:5 (w:v) in re-enforced 1.5 mL homogenizer tubes containing 50 mg glass beads. The samples were homogenized with 3 bursts of 60 seconds at a speed of 5 m/s. The homogenates were centrifuged at 9,000 *g* for 10 min. The protein concentration for each homogenate was determined using a Bradford assay. Two hundred µg of protein were extracted using ice-cold acetone precipitation (1/5; v/v). The protein pellet was dissolved in 100 µL of 50 mM TRIS-HCl buffer (pH 8) and the solution was mixed with a Disruptor Genie at maximum speed (2,800 rpm) for 15 minutes and sonicated to improve protein dissolution yield. The proteins were denatured by heating at 120˚C for 10 min using a heated reaction block. The solution was then allowed to cool down for 15 minutes. Proteins were reduced with 20 mM dithiothreitol (DTT) at 90˚C for 15 minutes. Then proteins were alkylated with 40 mM 2-Iodoacetamide (IAA) at room temperature for 30 min. Five µg of proteomic-grade trypsin was added at 37˚C for 24h. Protein digestion was quenched by adding 10 µL of a 1% TFA solution. Samples were centrifuged at 12,000 *g* for 10 min and 100 µL of the supernatant was transferred into injection vials for analysis.

Proteomic analysis

High-performance liquid chromatography was performed using a Thermo Scientific Vanquish FLEX UHPLC system (San Jose, CA, USA) using gradient elution along with a microbore

column (Thermo Biobasic C18 100 × 1 mm, with a particle size of 5 μm). The initial mobile phase condition consisted of acetonitrile and water (both fortified with 0.1% formic acid) at a ratio of 5:95. From 0 to 2 min, the ratio was maintained at 5:95. From 2 to 92 min, a linear gradient was applied up to a ratio of 40:60 and maintained for 3 min. The mobile phase composition ratio was reverted at the initial conditions and the column was allowed to re-equilibrate for 15 min. The flow rate was fixed at 50 μL/min and 5 μL of sample was injected. A Thermo Scientific Q Exactive Plus Orbitrap Mass Spectrometer (San Jose, CA, USA) was interfaced with the UHPLC system using a pneumatic assisted heated electrospray ion source. Nitrogen was used for sheath and auxiliary gases, and they were set at 10 and 5 arbitrary units. Auxiliary gas was heated to 200˚C. The heated ESI probe was set to 4,000 V and the ion transfer tube temperature was set to 300°C. MS detection was performed in positive ion mode and operating in TOP-10 Data Dependent Acquisition (DDA). A DDA cycle entailed one MS^1 survey scan (m/z 400-1500) acquired at 70,000 resolution (FWHM) and precursor ions meeting user defined criteria for charge state (i.e. z = 2, 3 or 4), monoisotopic precursor intensity (dynamic acquisition of MS^2 based TOP-10 most intense ions with a minimum $2x10^4$ intensity threshold) were selected for MS^2 acquisition. Precursor ions were isolated using the quadrupole (1.5 Da isolation width) and activated by HCD (28 NCE) and fragment ions were detected in the Orbitrap at 17,500 resolution (FWHM). Data were processed using Thermo Proteome Discoverer (version 2.4) in conjunction with SEQUEST using default settings unless otherwise specified. SEQUEST used a curated database consisting of FASTA sequences extracted from UniProt (i.e., *Mus musculus* TAXON ID 10090). The following Proteome Discoverer parameters were set: MS^1 tolerance of 10 ppm; MS^2 mass tolerance of 0.02 Da for Orbitrap detection; enzyme specificity was set as trypsin with two missed cleavages allowed; carbamidomethylation of cysteine was set as a fixed modification; and oxidation of methionine was set as a variable modification. The minimum peptide length was set to six amino acids, and

proteins identified by only one peptide were removed. Data sets were further analysed with Percolator [45]. Peptide-spectrum-matches (PSMs) and protein identification were filtered at 1% false discovery rate (FDR) threshold. For protein quantification and comparative analysis, we used the peak integration feature of the Proteome Discoverer 2.4 software [46]. For each identified protein, the average ion intensity of the unique peptides was used for protein abundance.

Data preparation

Microsoft Excel files, one per tissue were generated using Proteome Discoverer. The abundance ratios were generated from (MI)/(sham), (MI-RTX)/(sham) and (RTX)/(sham group). Proteins with UniProt accessions that mapped to a mouse and then a human symbol using the MGI human phenotype database [47] were retained provided they possessed valid expression levels across sets of biological replicates. In cases of multiple accessions mapping to the same human gene symbol, the accession with the best replicate data was retained. Since the number of replicates was at the lower limit of limma analysis with p-value estimation, we chose to just take the mean of replicates. In cases with a mixture of NA (not-available) values, they were only allowed when the other non-NA values were on the low end of the distribution for that group of samples. Data was next converted to delta-means, meant to represent the log fold change (LFC) of the difference between a mean of the values from one treatment group versus its Sham control group. These LFCs were assembled as a time series for all delta-Sham contrasts from all tissues and were hierarchically clustered with base R dist (euclidean) and hclust (ward.D) and cutree (k=24) [48]. Proteins from k-clusters with less that 100 genes in one tissue/treatment group were discarded and gene sets were assembled from the remaining genes for each treatment/sham contrast in each tissue.

Venn Diagrams

Venn diagrams were generated using the ggVennDiagram package [49] within the ggplot2 framework [50]. Input were string sets consisting of the gene symbols from each tissue as in Figure 1B or from each treatment after filtering for metabolism pathway genes that were also differentially expressed with ≥ 1.0 LFC for the 12 week and at least one of the 5 min or 24 hour time points as in Figure 5D.

Expression profile plots

The time course expression profile of each sample group after clustering and partitioning were presented using a custom ggplot2 script in R for the complete data set (Figure 2) or just genes involved in metabolism (Figure 4). When an LFC was NA for a time point, but the rest of the series had valid LFCs, the NA was replaced with 0 for clustering and plotting. Colors are arbitrary for each k-cluster. 21 of the 24 k-clusters are shown across the 4 tissues and only the 3 purple profiles are shared between the vagus and the spine. The other colors are in reds for the left ventricle, blues for the spine and greens for the medulla.

Enrichment and Heatmaps

An R interface to the API of the enrichR program was implemented in order to perform batch gene function database enrichment analyses for the large number of tissue/treatment groups we wanted to analyse against the Reactome [51] and Gene Ontology [52, 53] databases. All heatmaps were generated with the pheatmap package [54]. Returned result sets were filtered based on adjusted p-value ≤ 0.05 for the heatmaps in Figure 3 and Sup Figure 1 and by p-value ≤ 0.01 for Figure 5 A-C. Filtered data will show as grey cells in the heatmap. Colored cells are based on $\log_2$ (2 + CombinedScore), where the enrichR CombinedScore is defined as the log of the Fisher exact test p-value multiplied by the z-score computed by assessing the deviation from

the expected rank [37]. Samples are clustered based on these scores, depicted in the top dendrogram of each heatmap. Each enrichR result, even after p-value filtering, was too large to show in a heatmap, however many pathways in each result tended to overlap in terms of protein sub-set with similar functional descriptions. We therefore pooled each treatment's set of genes that were found in a particular pathway and formed a distance measure of overlap for hierarchical clustering (ward.D) and cutree: h = 500 for Reactome Figure 3A; h = 100 for GO cellular component; h = 75 for GO molecular function (Fig Sup 1A); h = 250 for GP biological process (Fig Sup 1B). Within each subtree, after cutree, the pathway with the best overall CombinedScores was chosen for display within the heatmap. This distance tree was also used in the clustering of the pathways, depicted in the left dendrogram of each heatmap.

Results

Detection of differentially regulated proteins

This study made use of a murine model for MI with and without RTX treatment to obtain proteomic data from four tissues over a four-point time course, as described in Figure 1A. MI and sham controls as well as RTX and saline treatments were performed at T0 and mouse tissues were isolated at 5 min (T1), 20 min (T2), 24 hr (T3) and 12-week (T4) time points. From each mouse we isolated the LV (red), the spine (blue), the MO (green) and vagus (purple). To identify the effects of the autonomic sensory afferents in response to MI, one group of MI animals concomitantly received restricted acute pericardial injection of RTX to obtain cardiac sensory afferent denervation (MI/RTX). We have previously shown detailed characteristics (e.g. survival rates, echocardiographic assessments, quantification of infarct zones, resting heart rate variability, QT and QTc intervals and morphological data) related with the model for HF used and long-term effects on heart and brain function [27]. We investigated changes in the proteome with our models by employing a previously established, label-free quantitative proteomic

approach. The activation of TRPV1 by an agonist will lead to an influx of cations tightly associated with TAC1 expression and the release of tachykinin peptides (e.g. Substance P). As shown in the supplementary Figure S1, the application of RTX triggered the expression and release of TAC1 proteins in the spinal cord (C1-C4) 20 min after treatment. The results are consistent with the agonist effects of RTX on TRPV1, producing an intense pungent effect. However, the MI/RTX group showed a different phenotype suggesting that the RTX pungent effect might be mitigated by molecular processes associated with the induction of MI. The four-way Venn diagram in Figure 1B shows the overlap and uniqueness in terms of protein content per tissue, looking at proteins that were detectable in at least 2/4 time points for at least 2/4 treatment groups, resulting in 1,499 proteins from spine samples, 1,197 from LV, 1,772 from MO and 514 from vagus. Each zone is coloured to indicate the areas with highest (light blue) to lowest number proteins (dark blue). In addition to the 301 unique proteins from the left ventricle and the 373 from the medulla, the largest shared groups include spine-medulla (532), spine-medulla-left ventricle (358) and the central zone, shared between all tissues (323). While one might expect the three neural tissues to have a large degree of proteomic overlap, it is surprising how many proteins were shared with the cardiac tissue supporting research suggesting an electrical nature of the heart and its connection with the nervous system.

Cluster analysis to identify co-regulated proteins

With the eventual goal of looking at tissue and treatment specific modulations in gene-functional pathways over the time course of the study, we assembled our expression data to resemble log2ratios with respect to sham at the four time points for each protein, retaining the tissue and treatment information for each time-course. Hierarchical clustering enabled us to refine a partitioning strategy in two steps. First, we manually adjusted the cutree k parameter, resulting in a k of 24, to obtain visually appealing clustered profiles when depicted as shown in

Figure 2. Second, we used a threshold of 100 waves per k-cluster per tissue/treatment group in order to remove outlier expression profiles that did not fit into any of the clusters that possessed the majority of the expression profiles, resulting in the retention of the 21 k-clusters shown in Figure 2. The spine retained 9 k-clusters, the MO and LV each had 6 and the vagus only 3, all of which were also retained by profiles from the spine (k2, k5 and k10). The complete data set, for all 24 clusters, is provided as a spreadsheet in Supplementary Data File 1 (encompassing 2375 proteins labelled with their relevant tissue and treatment groups).

Enrichment analysis of Gene Ontology and Reactome pathways

For each tissue/treatment group, all of the proteins from the clusters shown in Figure 2 were pooled and used to search the Gene Ontology (GO) and Reactome pathway databases with the enrichR program. Results were filtered on adjusted p-value ≤ 0.05 and then we used the $\log_2$ (2 + CombinedScore) to color the cells of the heatmaps shown in Figure 3. For tissue/treatment groups that did not statistically enrich a pathway, the cells are colored in grey. The samples are clustered based on this enrichR Combined Score and show that the effect in each Reactome pathway (Figure 3A) is more similar between the RTX and MI/RTX treatments than MI within each tissue, except for the vagus. In addition, the response of the spine and MO are more similar to each other than the LV or vagus, however it should be noted that the vagus scores suffered due to the lower overall number of proteins found in that tissue. The rows are clustered based on the degree of overlap between the enriched protein sets in each pathway. For the Reactome pathway database, we processed 12 enrichR results, one for each tissue/treatment group, each containing 131 to 342 different pathways with adjusted p-values ≤ 0.05. When merged together, 1,255 unique pathways were retained (Supplementary File 2). In order to condense these results for visualization by heatmap, we again used hierarchical clustering and cutree utilizing a distance measure based on overlapping protein content. This enables the heatmap to summarize

pathways that were functionally similar when they have largely overlapping protein sets. As shown in Figure 3A, there is a large degree of enrichment within Metabolism (Reactome identifier R-HSA-1430728, hereafter referred to as Metabolism) and Pyruvate metabolism and TCA cycle pathways in all groups. In addition, Apoptosis, Hemostasis, Vesicle-mediated transport and Signalling by NGF were significant in all groups and Adaptive Immune System was found everywhere except in the vagus. Due to the shared disturbance in metabolism pathways, we next looked at GO cell component (GO:CC) in the same manner and can hypothesize that a large part of the response we found through these proteomic experiments is due to changes in the mitochondria of the cells. As shown in Figure 3B, we found GO:CC categories that correspond to the vesicle-related Reactome pathways such as vesicle, neuron projection, membrane raft and cell-cell junction to name a few. Combined with the high scores from cytoskeletal pathways, it is clear that these treatment groups all underwent massive changes in cellular signalling networks. The GO molecular function (GO:MF) and biological process (GO:BP) databases were also queried (Supplementary Figures S2A and S2B, respectively) and revealed additionally that many of the proteins under examination are involved in RNA binding and protein folding/stability (GO:MF) and further support the role of metabolism and immunity (GO:BP pyruvate metabolic process and neutrophil mediated immunity). Complete tables of all enrichR results are also available as Supplementary File 2.

Cluster analysis to identify association between pathways in regulatory networks

To further investigate the findings regarding Metabolism at the protein level. We extracted the profiles shown in Figure 2 for each protein that was found in the Reactome Metabolism pathway (Figure 4). In this way, it is clear that while each of the treatments modulates metabolism via a large number of common proteins, the profile over the time course is different based on each treatment. Essentially, in all 3 treatments the proteins from metabolism are increased immediately in T1 as compared to Sham. In RTX, the protein levels gradually resume to sham

levels at 24 h in all tissues. In the LV (Figure 4A) k9 and k13 appear to be MI specific profiles. MI/RTX responses concentrate almost uniquely in k24 while the RTX response is most evident in k6 and k18. These data show that while Metabolism includes a very large group of proteins, further dissecting the responses show how the LV had a treatment specific response. Figure 4B represents the waveforms of the metabolic proteins in the spine in all three treatments. Certain profiles such as k3 and k10 may reflect an MI response whereas k4, k19, k20 and k21 show a tendency to be elicited by RTX. The vagus showed that the k5 cluster was most evident in MI while MI/RTX showed an increased tendency in k10. RTX treatment had little effect on the metabolic profiles of the vagus. The MO also showed that k16 and k22 may be MI specific, while k23 is an intriguing profile solicited strongly by RTX, absent from MI/RTX, but a small subset of proteins share a similar profile in MI.

Treatment specific enrichment analysis of Reactome pathways

Finally, we wanted to focus on any treatment specific effects that persist across all tissues and involve proteins with the largest degree of fold change versus the Sham controls. First, we selected proteins with absolute $\log_2$fold change ≥ 1 at 12 weeks and at least one of the following timepoints: 5 min or 24 h. We repeated the enrichR analysis of the Reatome database looking at each treatment group separately, shown in Figure 5 (A: MI, B: MI/RTX, C: RTX). Heatmaps were prepared as in Figure 3, however due to smaller number of proteins per group, we relied on a non-adjusted p-value ≤ 0.01 for these analyses. With the filtering of proteins that did not have long term changes with respect to sham, we found that MI retained selection of Metabolism over all tissues but that TCA cycle pathways were only retained in the LV (Figure 5A). MI/RTX and RTX treatment likewise have long term changes in Metabolism in all tissues however the TCA cycle is not significant in the MO with MI/RTX (Fig 5B) and RTX (Fig 5C). Finally, all proteins from the Metabolism pathway selected as described for the Figure 5

heatmaps were placed into a Venn diagram (Figure 5D) in order to show that while there are a lot of shared proteins, 98 from all three treatments and 133 shared between MI and MI/RTX, there are also more unique RTX proteins (57) and unique MI/RTX proteins (40) than there are shared only between RTX and MI/RTX (26).

Discussion

In order to better understand the complexity behind the interactions between the heart and the nervous system in HF, we undertook a large proteomic analysis of four tissues over a 12-week time course using combinations of MI and RTX treatments. By 12 weeks, the adverse effects of MI have been compensated for by RTX treatment and by including earlier time points in our analysis, we were able to monitor how these various treatments affected these tissues at 5 min, 20 min, 24 h as well as after 12 weeks. We were particularly interested in the early timepoints as to date RTX application to the heart in order to rescue HF progression following infarction is often concurrent with the induction of MI [22–27]. Application of RTX elicits an immediate excitation of TRPV1 expressing sensory neurons followed by a blocking effect whereby neurons can no longer sense the stimuli, which then ultimately leads to neurodegeneration of the sensory fibers [56, 57]. While we can observe a rapid and important response in the spine following RTX treatment, we further confirmed that the excitation response was prompted in the spine at 20 min by an up-regulation of TAC1 (Figure S1) leading to the release of pronociceptive neuropeptides (i.e. SP and NKA). Further, we know from our previous studies that RTX abolished the cardiac sensory fibers at 12 weeks post infarction [27]. In order to analyse this large dataset, we consolidated all the time points into waveforms that could be partitioned into clusters of genes with similar expression profiles over the time course by hierarchical clustering. One interesting observation in our data was that RTX induced a response in the LV even though it is commonly referred to as being benign in the heart [26, 30,

43]. Our data here is consistent with novel findings from the development and use of heterozygous TRPV1$^{-Cre+/-,tdTomato\ flox/flox+/-}$ mice [58], which demonstrated that while TRPV1 channels are mostly expressed in cardiac nerve endings they are also found in the vessels of the mouse heart [58]. As such, we need to keep in mind that RTX may elicit its effects through blood vessels in addition to the cardiac afferent nerves. Nonetheless, our findings with RTX alone show a stimulation in all tissues that essentially return to baseline levels over time and concur with physiological findings [22–27]. Moreover, we see that application of RTX to the heart also elicited long-term adaptations in the MO and in the vagus nerve. These findings, while surprising, are consistent with RTX induction of long-lasting sensory neuron desensitization to achieve permanent analgesia [56, 57], which may represent the underlying adaptive processes supporting analgesia.

The waveform profiles presented in Figure 2 obtained for the combined MI/RTX treatment were paradoxical and tissue dependent. For example, we found that the MI/RTX response closely resembled that of MI for the LV, but in the spine the response was similar to that observed in RTX. This is consistent with the notion that RTX prompts a response in cardiac afferent nerves that transmit information through the spinal cord [21, 26]. Profiles of proteomic responses in spines isolated from mice in the MI/RTX treatment group showed a similar response curve to RTX animals, but with lower response amplitude. These findings may indicate a dampening of the RTX response in the spine in conjunction with MI; but further study will be required to understand this observation given that spine isolated from MI treated animals showed relatively low responses throughout all time points. The responses observed in the vagus nerve samples per treatment were surprising. The effect of MI on the vagus has not been extensively studied, however left vagal nerve stimulation following MI has been shown to ameliorate cardiac function in a canine model [59]. The waveform in MI was similar to that observed for MI/RTX but the response was more pronounced at early time points. These

findings suggest that the vagus is solicited early after MI and that concurrently blocking the sympathoexcitatory TRPV1+ cardiac neurons result in a reduced engagement of the vagus following MI.

Once all the time points were consolidated into waveforms and partitioned into clusters of genes with similar profiles over the time course by hierarchical clustering, we sought to functionally characterize the gene sets within each Tissue/Treatment group by enrichment analysis with the Reactome database. Surprisingly, the top pathway found in all tissues and treatments was Metabolism (e.g. R-HSA-1430728). It encompasses a complex network of chemical reactions and represents the largest and best characterized biomolecular network whereby the function of the underlying genes and proteins are well known. To study the proteomic changes associated with MI and RTX in the neuronal tissues connecting the heart to the brain, we thought to push genes specifically associated to Metabolism to the side and try to pick apart many of the other aspects of the results that had more precise functional descriptions. However, upon routinely finding metabolism associated genes at the statistical top of every analysis, we wanted to further explore the implications. Maladaptive energetics of cardiac tissue contribute to the pathophysiology of the failing heart [2, 5, 7]. More and more, we are learning of the complex metabolic processes associated with myocardial metabolic failure and systemic metabolic regulation has been found to contribute both to major symptoms and to disease progression [40, 60]. As such, HF is now defined as a systemic, multi-organ syndrome associated with metabolic failure [61]. One of the associations made between altered metabolism and HF include the activation of the neurohumoral system; which is the chronic activation of the sympathetic nervous system and the Renin-Angiotensin-Aldosterone System (RAAS) [62]. Moreover, in the last decade, the notion of cross-talk between the infarcted heart and peripheral tissues is of considerable interest within the research community [2, 4, 55, 63–66]. Metabolic dysregulation in the liver, skeletal muscle and adipose tissues following myocardial infarction has been shown

[2], and genome-wide transcriptomic analysis on tissue samples obtained 6- and 24-h post-MI demonstrated that tissue-specific biological networks showed a dysregulation in multiple biological processes (including immune system, mitochondrial dysfunction, fatty-acid beta-oxidation as well as RNA and protein processing) across multiple tissues, in particular in the liver.

We then made use of the three Gene Ontology databases to further confirm the functional changes in the cells of these tissues exposed to these various treatments. While the cellular component database from Gene Ontology suggests that proteomic changes in metabolism are localized within the mitochondria, previously reported in cardiomyocytes and HF [67], certain metabolic pathways have recently been found to be functional in the cytoplasm, distinct from the larger mitochondrial structures [68]. In either case, our discoveries that the protein components of mitochondria are being modified both by MI and RTX in the LV, spine, MO and vagus, could be explained based on merely the energetic needs of the tissues that propagate neural electrical- and chemical- signals back and forth within the tissues that connect the heart and the brain. It is quite clear that there is a large up-regulated peak at 20 minutes everywhere in this dataset as revealed in Figure 2. Interestingly, in the LV, the majority of the proteins are detected at higher levels in Sham versus all three treatment groups. The same can be said for the spine and the vagus. However, the MO shows the exact opposite and at 5 minutes, most proteins are up in the treatment groups with respect to their Sham counterparts. Looking at long term changes, over 12 weeks, these same proteins are down again for the most part in the left ventricle, however most of them move upwards by 12 weeks in spine and vagus. The MO continues to trend downwards at 12 weeks, despite their initial up-regulation at 5 minutes.

In addition to metabolism and related pathways such as TCA cycle, we found Reactome pathways such as vesicles, apoptosis, hemostasis and signaling by nerve growth factor (NGF)

(Figure 3A). While it is expected to find such functional pathways in the neural tissues, it was less expected for the LV. The fact that these pathways were also found in the heart may further suggest shared regulatory mechanisms for adaptation to MI and RTX in all tissues via neuronal pulse communications [69, 70]. We can also reveal that cadherin binding is consistently enriched everywhere (Figure S2A), in addition to RNA binding and protein degradation pathways, in agreement with previously published works [2]. The expected enrichment in muscle contraction was also seen in most all other samples and neutrophil mediated immunity was found in all tissues and treatments (Figure S2B), suggesting an additional layer of complexity to the response to MI and RTX. There were also pathways related to supramolecular fiber organization and actin/tubulin binding as well as many hits to cytoskeletal and actin-related categories with the cellular component database (Figure 3B). Taken together, we see that there is both short- and long-term disturbances in pathways not only related to mitochondria, but also the cytoskeleton, vesicles and various signaling pathways.

Performing an additional analysis by partitioning the overall proteome as shown in Figure 2 with only the profiles of genes from the Reactome Metabolism pathway, we noted that a principal proteomic signature, depicted as k-clusters, are proportionately represented within the proteins from the metabolism subset (Figure 4). When we further refined the proteome under study by selecting only proteins with a 1.0 log fold change at 12 weeks and an additional time point of either 5 minutes or 24 hours, we still found metabolism to be the only consistent pathway for all treatments (Figure 5A, B, C). This subset of proteins involved in metabolism also showed a balanced mixture of shared and distinct proteins across the MI, RTX and MI/RTX treatment groups (Figure 5D).

One can imagine that the cyclical transport of ions across membranes to generate neural signals is an energy intensive process. The spine, MO and vagus are all considered to be largely post-

mitotic cellular networks that function to transmit signals by the ATP intensive process of pushing ions across the membrane against the gradient. It is plausible that this network of post-mitotic cells makes use of mitochondria as adaptive and receptive component to fine tune neuronal behaviour in times of need. The triggering of MI results in a large change in the signaling between the heart and the brain [71]. The response at the interface of the heart is more similar to the connected neuronal network that we anticipated. On the other hand, the MO appears to make use of a large number of similar proteins with these neuro-connective tissues in terms of its adaptive response to signals such as MI and RTX. The precise injection of RTX in the pericardium to interact with epicardial sensory neurons ablates signaling from the heart to the brain [22, 26, 27]. There is an immense proteomic impact with RTX treatment alone on all tissues and there is a large overlap in terms of functional pathways and individual proteins shared with the MI treatment groups. While this is an important and surprising finding, we cannot discern at a proteomic level exactly how RTX treatment alleviates the symptoms associated with MI. However, our findings suggest that mitochondria plays an important role. Not only can one suppose that the difference in signaling associated with MI and RTX require different energy stores, one can also imagine the mitochondria as low-level signaling sensors for the intracellular health of the cells participating in the neuronal connection. The mitochondria, as they adapt, can trigger response adaptation in the cytoskeletal network as well as all manner of signaling apparatus that manage vesicle traffic and interpretation of extracellular stimuli [72, 73]. One can even envision that the electromagnetic pulses of the tissue are sensed by the H^+ gradients inside the mitochondria and that the first level of cellular detection to changes in neuronal pulse frequency are the mitochondria due to the proton gradients that grow adapted to whatever frequency is present.

It is important to recognize certain limitations associated with these experiments. For example,

we did not measure infarct size at the early time points and prior to the collection of tissues at the immediate time point, animals were under isoflurane inhalant and ventilated; both of which have effects on cardiac and nervous system function [74, 75] . Additionally, only proteomic data was analysed in this research, hence the sensitivity might be limited especially for the 5 min time points. Since we focussed our research on dissected portions of each tissue, observed changes may reflect only a portion of the systemically changing events. Our bioinformatic analyses revealed a high degree of overlap between all tissues and treatments heavily implicating metabolism and mitochondrial function. Despite the overlap in terms of proteins identified and their respective functional pathways, there are clearly very different expression profiles over time in the tissues studied based on the treatment imposed.

Conclusion

We provide central pathways for systemic metabolic allostasis to cardiac dysfunction and add to the important growing body of evidence for systemic, integrative pathophysiological responses regulated by cardiac sensory fibres in HF. These results should aid in establishing future experiments to dissect how metabolic changes in neuronal tissues can effectively ameliorate the negative physiological effects of MI via RTX application. Efforts towards developing effective treatments for HF have shown limited efficacy at best, with no efficient cure to this day. Our work helps to uncover certain differential metabolic constituents involved in the link between cardiac metabolism and the peripheral and central nervous systems that are potential targets for future therapies. Therapeutics combining neuroprotective aspects in addition to modulation of metabolic activities may offer better outcomes for HF patients.

Acknowledgments

We acknowledge core support from Animal facility ANEXPLO, CREFRE US006 Rangueil,

and in particular Xavier Sudre for his expertise. This work was funded by the Foundation de France grant number RAF18002BBA awarded to Dina N Arvanitis. The proteomic investigations were funded by the National Sciences and Engineering Research Council of Canada (F. Beaudry discovery grant no. RGPIN-2020-05228). Laboratory equipment was funded by the Canadian Foundation for Innovation (CFI) and the Fonds de Recherche du Québec (FRQ), the Government of Quebec (F. Beaudry CFI John R. Evans Leaders grant no. 36706). F. Beaudry is the holder of the Canada Research Chair in metrology of bioactive molecule and target discovery (grant no. CRC-2021-00160). This research was undertaken, partly, thanks to funding from the Canada Research Chairs Program. Ph.D. scholarships were awarded to J. Ben Salem from the Fonds de Recherche du Québec - Santé (scholarship no. 302490) and from the Université de Montréal.

Conflict of interest

The authors declare no conflicts of interest.

Data availability

The data that support the findings from this study are available from the corresponding author upon reasonable request

References

1. Savarese G, Division of Cardiology, Department of Medicine, Karolinska Insitutet, Stockholm, Sweden, Department of Cardiology, Karolinska University Hospital, Stockholm, Sweden, et al (2017) Global Public Health Burden of Heart Failure. Cardiac Failure Review 03:7. https://doi.org/10.15420/cfr.2016:25:2

2. Arif M, Klevstig M, Benfeitas R, et al (2021) Integrative transcriptomic analysis of tissue-specific metabolic crosstalk after myocardial infarction. eLife 10:e66921. https://doi.org/10.7554/eLife.66921

3. Doran S, Arif M, Lam S, et al (2021) Multi-omics approaches for revealing the complexity of cardiovascular disease. Briefings in Bioinformatics 22:bbab061. https://doi.org/10.1093/bib/bbab061

4. Katz SD (2018) Pathophysiology of Chronic Systolic Heart Failure. A View from the Periphery. Annals ATS 15:S38–S41. https://doi.org/10.1513/AnnalsATS.201710-789KV

5. Muqtadar H, Testai FD, Gorelick PB (2012) The Dementia of Cardiac Disease. Curr Cardiol Rep 14:732–740. https://doi.org/10.1007/s11886-012-0304-8

6. Amare AT, Schubert KO, Klingler-Hoffmann M, et al (2017) The genetic overlap between mood disorders and cardiometabolic diseases: a systematic review of genome wide and candidate gene studies. Transl Psychiatry 7:e1007–e1007. https://doi.org/10.1038/tp.2016.261

7. Doehner W, Ural D, Haeusler KG, et al (2018) Heart and brain interaction in patients with heart failure: overview and proposal for a taxonomy. A position paper from the Study Group on Heart and Brain Interaction of the Heart Failure Association: Heart and brain interaction in heart failure. Eur J Heart Fail 20:199–215. https://doi.org/10.1002/ejhf.1100

8. Tahsili-Fahadan P, Geocadin RG (2017) Heart–Brain Axis: Effects of Neurologic Injury on Cardiovascular Function. Circ Res 120:559–572. https://doi.org/10.1161/CIRCRESAHA.116.308446

9. Park CM, Williams ED, Chaturvedi N, et al (2017) Associations Between Left Ventricular Dysfunction and Brain Structure and Function: Findings From the SABRE (Southall and Brent Revisited) Study. JAHA 6:. https://doi.org/10.1161/JAHA.116.004898

10. Suzuki H, Sumiyoshi A, Matsumoto Y, et al (2015) Structural abnormality of the hippocampus associated with depressive symptoms in heart failure rats. NeuroImage 105:84–92. https://doi.org/10.1016/j.neuroimage.2014.10.040

11. Ovsenik A, Podbregar M, Fabjan A (2021) Cerebral blood flow impairment and cognitive decline in heart failure. Brain Behav 11:. https://doi.org/10.1002/brb3.2176

12. Tromp J, Westenbrink BD, Ouwerkerk W, et al (2018) Identifying Pathophysiological Mechanisms in Heart Failure With Reduced Versus Preserved Ejection Fraction. Journal

of the American College of Cardiology 72:1081–1090. https://doi.org/10.1016/j.jacc.2018.06.050

13. Elam M, Sverrisdottir YB, Rundqvist B, et al (2003) Pathological sympathoexcitation: how is it achieved? Acta Physiologica Scandinavica 177:405–411. https://doi.org/10.1046/j.1365-201X.2003.01080.x

14. May CN, Frithiof R, Hood SG, et al (2010) Specific control of sympathetic nerve activity to the mammalian heart and kidney: Control of cardiac and renal sympathetic nerve activity. Experimental Physiology 95:34–40. https://doi.org/10.1113/expphysiol.2008.046342

15. Zhang DY, Anderson AS (2014) The Sympathetic Nervous System and Heart Failure. Cardiology Clinics 32:33–45. https://doi.org/10.1016/j.ccl.2013.09.010

16. Despas F, Detis N, Dumonteil N, et al (2009) Excessive sympathetic activation in heart failure with chronic renal failure: role of chemoreflex activation: Journal of Hypertension 27:1849–1854. https://doi.org/10.1097/HJH.0b013e32832e8d0f

17. Despas F, Lambert E, Vaccaro A, et al (2012) Peripheral chemoreflex activation contributes to sympathetic baroreflex impairment in chronic heart failure: Journal of Hypertension 30:753–760. https://doi.org/10.1097/HJH.0b013e328350136c

18. Franchitto N, Despas F, Labrunee M, et al (2013) Cardiorenal anemia syndrome in chronic heart failure contributes to increased sympathetic nerve activity. International Journal of Cardiology 168:2352–2357. https://doi.org/10.1016/j.ijcard.2013.01.023

19. Kishi T (2016) Deep and future insights into neuromodulation therapies for heart failure. Journal of Cardiology 68:368–372. https://doi.org/10.1016/j.jjcc.2016.05.010

20. Kingma JG, Simard D, Rouleau JR (2017) Influence of cardiac nerve status on cardiovascular regulation and cardioprotection. WJC 9:508. https://doi.org/10.4330/wjc.v9.i6.508

21. Zahner MR, Li D-P, Chen S-R, Pan H-L (2003) Cardiac vanilloid receptor 1-expressing afferent nerves and their role in the cardiogenic sympathetic reflex in rats. The Journal of Physiology 551:515–523. https://doi.org/10.1113/jphysiol.2003.048207

22. Coote JH, Chauhan RA (2016) The sympathetic innervation of the heart: Important new insights. Autonomic Neuroscience 199:17–23. https://doi.org/10.1016/j.autneu.2016.08.014

23. Chen W-W, Xiong X-Q, Chen Q, et al (2015) Cardiac sympathetic afferent reflex and its implications for sympathetic activation in chronic heart failure and hypertension. Acta Physiol 213:778–794. https://doi.org/10.1111/apha.12447

24. Yoshie K, Rajendran PS, Massoud L, et al (2020) Cardiac TRPV1 afferent signaling promotes arrhythmogenic ventricular remodeling after myocardial infarction. JCI Insight 5:e124477. https://doi.org/10.1172/jci.insight.124477

25. Senador Danielle, Kaur Jasdeep, Sala-Mercardo Javier A., et al (2017) Pharmacological cardiac sympathetic afferent denervation in pacing-induced heart failure. The FASEB

Journal 31:p.884.2-844.2. https://doi.org/10.1096/fasebj.31.1_supplement.844.2

26. Wang H-J, Wang W, Cornish KG, et al (2014) Cardiac Sympathetic Afferent Denervation Attenuates Cardiac Remodeling and Improves Cardiovascular Dysfunction in Rats With Heart Failure. Hypertension 64:745–755. https://doi.org/10.1161/HYPERTENSIONAHA.114.03699

27. Kermorgant M, Ben Salem J, Iacovoni JS, et al (2021) Cardiac sensory afferents modulate susceptibility to anxio-depressive behaviour in a mouse model of chronic heart failure. Acta Physiol 231:. https://doi.org/10.1111/apha.13601

28. Foreman RD (1999) MECHANISMS OF CARDIAC PAIN. Annu Rev Physiol 61:143–167. https://doi.org/10.1146/annurev.physiol.61.1.143

29. Cechetto DF (2014) Cortical control of the autonomic nervous system: Cortical autonomic control. Experimental Physiology 99:326–331. https://doi.org/10.1113/expphysiol.2013.075192

30. Wu Y, Hu Z, Wang D, et al (2020) Resiniferatoxin reduces ventricular arrhythmias in heart failure via selectively blunting cardiac sympathetic afferent projection into spinal cord in rats. European Journal of Pharmacology 867:172836. https://doi.org/10.1016/j.ejphar.2019.172836

31. Capilupi MJ, Kerath SM, Becker LB (2020) Vagus Nerve Stimulation and the Cardiovascular System. Cold Spring Harb Perspect Med 10:a034173. https://doi.org/10.1101/cshperspect.a034173

32. Dusi V, De Ferrari GM, Mann DL (2020) Cardiac Sympathetic-Parasympathetic Interaction. JACC: Basic to Translational Science 5:811–814. https://doi.org/10.1016/j.jacbts.2020.07.004

33. Bibevski S, Dunlap ME (2011) Evidence for impaired vagus nerve activity in heart failure. Heart Fail Rev 16:129–135. https://doi.org/10.1007/s10741-010-9190-6

34. Li M, Zheng C, Kawada T, et al (2019) Chronic vagal nerve stimulation exerts additional beneficial effects on the beta-blocker-treated failing heart. J Physiol Sci 69:295–303. https://doi.org/10.1007/s12576-018-0646-0

35. Liu J-J, Huang N, Lu Y, et al (2015) Improving vagal activity ameliorates cardiac fibrosis induced by angiotensin II: in vivo and in vitro. Sci Rep 5:17108. https://doi.org/10.1038/srep17108

36. Zannad F, De Ferrari GM, Tuinenburg AE, et al (2015) Chronic vagal stimulation for the treatment of low ejection fraction heart failure: results of the NEural Cardiac TherApy foR Heart Failure (NECTAR-HF) randomized controlled trial. European Heart Journal 36:425–433. https://doi.org/10.1093/eurheartj/ehu345

37. Chen EY, Tan CM, Kou Y, et al (2013) Enrichr: interactive and collaborative HTML5 gene list enrichment analysis tool. BMC Bioinformatics 14:128. https://doi.org/10.1186/1471-2105-14-128

38. Kuleshov MV, Jones MR, Rouillard AD, et al (2016) Enrichr: a comprehensive gene set

enrichment analysis web server 2016 update. Nucleic Acids Res 44:W90–W97. https://doi.org/10.1093/nar/gkw377

39. Xie Z, Bailey A, Kuleshov MV, et al (2021) Gene Set Knowledge Discovery with Enrichr. Current Protocols 1:. https://doi.org/10.1002/cpz1.90

40. Pullen AB, Kain V, Serhan CN, Halade GV (2020) Molecular and Cellular Differences in Cardiac Repair of Male and Female Mice. JAHA 9:. https://doi.org/10.1161/JAHA.119.015672

41. Brar TK (2015) Effect of Different Phases of Menstrual Cycle on Heart Rate Variability (HRV). JCDR. https://doi.org/10.7860/JCDR/2015/13795.6592

42. Mena F, Benoit L (2019) Molecular programs underlying differences in the expression of mood disorders in males and females. Brain Research 1719:89–103. https://doi.org/10.1016/j.brainres.2019.05.016

43. Wang H-J, Rozanski GJ, Zucker IH (2017) Cardiac sympathetic afferent reflex control of cardiac function in normal and chronic heart failure states: Cardiac sympathetic afferent reflex control. The Journal of Physiology 595:2519–2534. https://doi.org/10.1113/JP273764

44. Yoshie K, Rajendran PS, Massoud L, et al (2018) Cardiac vanilloid receptor-1 afferent depletion enhances stellate ganglion neuronal activity and efferent sympathetic response to cardiac stress. American Journal of Physiology-Heart and Circulatory Physiology 314:H954–H966. https://doi.org/10.1152/ajpheart.00593.2017

45. The M, MacCoss MJ, Noble WS, Käll L (2016) Fast and Accurate Protein False Discovery Rates on Large-Scale Proteomics Data Sets with Percolator 3.0. J Am Soc Mass Spectrom 27:1719–1727. https://doi.org/10.1007/s13361-016-1460-7

46. Orsburn BC (2021) Proteome Discoverer—A Community Enhanced Data Processing Suite for Protein Informatics. Proteomes 9:15. https://doi.org/10.3390/proteomes9010015

47. Smith CL, Eppig JT (2009) The mammalian phenotype ontology: enabling robust annotation and comparative analysis. WIREs Syst Biol Med 1:390–399. https://doi.org/10.1002/wsbm.44

48. R Foundation for Statistical Computing R Core Team (2014). R: A language and environment for statistical computing. Vienna, Austria

49. Gao C-H, Yu G, Cai P (2021) ggVennDiagram: An Intuitive, Easy-to-Use, and Highly Customizable R Package to Generate Venn Diagram. Front Genet 12:706907. https://doi.org/10.3389/fgene.2021.706907

50. Wickham H (2009) ggplot2. Springer New York, New York, NY

51. Jassal B, Matthews L, Viteri G, et al (2019) The reactome pathway knowledgebase. Nucleic Acids Research gkz1031. https://doi.org/10.1093/nar/gkz1031

52. Ashburner M, Ball CA, Blake JA, et al (2000) Gene Ontology: tool for the unification of

biology. Nat Genet 25:25–29. https://doi.org/10.1038/75556

53. The Gene Ontology Consortium, Carbon S, Douglass E, et al (2021) The Gene Ontology resource: enriching a GOld mine. Nucleic Acids Research 49:D325–D334. https://doi.org/10.1093/nar/gkaa1113

54. Raivo Kolde (2019) pheatmap: Pretty Heatmaps

55. Li D, Mabrouk OS, Liu T, et al (2015) Asphyxia-activated corticocardiac signaling accelerates onset of cardiac arrest. Proc Natl Acad Sci USA 112:E2073–E2082. https://doi.org/10.1073/pnas.1423936112

56. Sapio MR, Neubert JK, LaPaglia DM, et al (2018) Pain control through selective chemo-axotomy of centrally projecting TRPV1+ sensory neurons. Journal of Clinical Investigation 128:1657–1670. https://doi.org/10.1172/JCI94331

57. Jeffry JA, Yu S-Q, Sikand P, et al (2009) Selective Targeting of TRPV1 Expressing Sensory Nerve Terminals in the Spinal Cord for Long Lasting Analgesia. PLoS ONE 4:e7021. https://doi.org/10.1371/journal.pone.0007021

58. Hong J, Lisco AM, Rudebush TL, et al (2020) Identification of Cardiac Expression Pattern of Transient Receptor Potential Vanilloid Type 1 (TRPV1) Receptor using a Transgenic Reporter Mouse Model. Neuroscience Letters 737:135320. https://doi.org/10.1016/j.neulet.2020.135320

59. Zhao S, Dai Y, Ning X, et al (2021) Vagus Nerve Stimulation in Early Stage of Acute Myocardial Infarction Prevent Ventricular Arrhythmias and Cardiac Remodeling. Front Cardiovasc Med 8:648910. https://doi.org/10.3389/fcvm.2021.648910

60. Doehner W, Frenneaux M, Anker SD (2014) Metabolic Impairment in Heart Failure. Journal of the American College of Cardiology 64:1388–1400. https://doi.org/10.1016/j.jacc.2014.04.083

61. Rosano GM, Department of Medical Sciences, IRCCS San Raffaele Pisana, Rome, Italy, Vitale C, Department of Medical Sciences, IRCCS San Raffaele Pisana, Rome, Italy (2018) Metabolic Modulation of Cardiac Metabolism in Heart Failure. Cardiac Failure Review 4:99. https://doi.org/10.15420/cfr.2018.18.2

62. Zucker IH, Xiao L, Haack KKV (2014) The central renin–angiotensin system and sympathetic nerve activity in chronic heart failure. Clinical Science 126:695–706. https://doi.org/10.1042/CS20130294

63. Philippou A, Xanthis D, Chryssanthopoulos C, et al (2020) Heart Failure–Induced Skeletal Muscle Wasting. Curr Heart Fail Rep 17:299–308. https://doi.org/10.1007/s11897-020-00468-w

64. Jahng JWS, Song E, Sweeney G (2016) Crosstalk between the heart and peripheral organs in heart failure. Exp Mol Med 48:e217–e217. https://doi.org/10.1038/emm.2016.20

65. Van Linthout S, Tschöpe C (2017) Inflammation – Cause or Consequence of Heart Failure or Both? Curr Heart Fail Rep 14:251–265. https://doi.org/10.1007/s11897-017-

0337-9

66. Kemp CD, Conte JV (2012) The pathophysiology of heart failure. Cardiovascular Pathology 21:365–371. https://doi.org/10.1016/j.carpath.2011.11.007

67. Nakamura M, Sadoshima J (2018) Mechanisms of physiological and pathological cardiac hypertrophy. Nat Rev Cardiol 15:387–407. https://doi.org/10.1038/s41569-018-0007-y

68. Fuller GG, Kim JK (2021) Compartmentalization and metabolic regulation of glycolysis. Journal of Cell Science 134:jcs258469. https://doi.org/10.1242/jcs.258469

69. Franzoso M, Zaglia T, Mongillo M (2016) Putting together the clues of the everlasting neuro-cardiac liaison. Biochimica et Biophysica Acta (BBA) - Molecular Cell Research 1863:1904–1915. https://doi.org/10.1016/j.bbamcr.2016.01.009

70. Pius-Sadowska E, Machaliński B (2021) Pleiotropic activity of nerve growth factor in regulating cardiac functions and counteracting pathogenesis. ESC Heart Failure 8:974–987. https://doi.org/10.1002/ehf2.13138

71. Méloux A, Béjot Y, Rochette L, et al (2020) Brain-Heart Interactions During Ischemic Processes: Clinical and Experimental Evidences. Stroke 51:679–686. https://doi.org/10.1161/STROKEAHA.119.027732

72. Miller MA, Zachary JF (2017) Mechanisms and Morphology of Cellular Injury, Adaptation, and Death. In: Pathologic Basis of Veterinary Disease. Elsevier, pp 2-43.e19

73. Moore AS, Holzbaur EL (2018) Mitochondrial-cytoskeletal interactions: dynamic associations that facilitate network function and remodeling. Current Opinion in Physiology 3:94–100. https://doi.org/10.1016/j.cophys.2018.03.003

74. Constantinides C, Mean R, Janssen BJ (2011) Effects of isoflurane anesthesia on the cardiovascular function of the C57BL/6 mouse. ILAR J 52:e21-31

75. Janssen BJA, De Celle T, Debets JJM, et al (2004) Effects of anesthetics on systemic hemodynamics in mice. American Journal of Physiology-Heart and Circulatory Physiology 287:H1618–H1624. https://doi.org/10.1152/ajpheart.01192.2003

Figure Legends

Figure 1. A) Illustrated workflow of the experimental protocol used in the study. Adult male C57BL6 males (n=6/group/timepoint) were subject to acute irreversible myocardial infarction in the presence of pericardial targeted injections of RTX or saline. The following time points T1 (5 min), T2 (20 min), T3 (24h) and T4 (12-weeks) from the left ventricle (LV), spine, vagus and medulla oblangata (MO) were isolated and processed for mass spectrometry. B) Degree of proteomic overlap between the four tissues under investigation. Tryptic peptides with a valid signal retained after initial filtering in at least 2 of 4 time-points and 2 of 4 treatments in at least 2/4 time points resulting in 1,499 proteins from spine samples, 1,197 from LV, 1,772 from MO and 514 from vagus. Area colour brightness is used to indicate areas with the highest number of overlapping proteins as the lightest shade of blue. In addition to the 301 unique proteins from the left ventricle and the 373 from the medulla, the largest shared groups include spine-medulla (532), spine-medulla-left ventricle (358) and the central zone, shared between all tissues (323).

Figure 2. All protein expression time series, expressed as delta-means with respect to Sham controls, were partitioned by hierarchical clustering (kmeans, k = 24). Each k-cluster is arbitrarily assigned a specific colour, with LV in reds, Spine in blues, MO in greens and the 3 clusters shared between Spine and Vagus in purples. K-clusters with less than 100 proteins from any treatment group were not retained, leading to 21 out of 24 k-clusters being shown. Profiles are displayed with time on the x-axis and the delta-mean with respect to sham on the y-axis. A) LV 6 k-clusters, B) Spine 9 k-clusters, C) Vagus 3 k-clusters, D) MO 6 k-clusters..

Figure 3. Functional characterization of the sets of proteins found for each tissue/treatment group were assessed using EnrichR and the Reactome (A) and Gene Ontology cellular component (B) database. Only pathways with adjusted p-value ≤ 0.05 were retained for downstream analysis. Within the heatmap, the cells are colored based on $\log_2$ (2 + enrichR-CombinedScore) and the sample groups are clustered based on these values. The rows are clustered based on the degree of overlap of the proteins within each set that led to enrichment of each pathway. Clustering and cutree were used to group similar pathways (h=500 for Reactome and h=100 for GO:CC) and the pathway with the best CombinedScores within each cluster were selected for visualization in the heatmap.

Figure 4. Wave profiles representing only the proteins identified in the Metabolism Reactome pathway for the LV, Spine, vagus and MO extracted from the profiles shown in Figure 2. A. Differing profiles are observed in the LV for MI and MI/RTX. k9 and k13 appear to be MI specific profiles while MI/RTX protein response profiles concentrated in k24 and RTX response is most evident in k6 and k18. B. In the spine MI response is observed in k3 and k10 and RTX

appears responsible for protein responses observed in k4, k19 k20 and k21. C. Proteomic responses in the vagus showed that the k5 cluster is MI dependent and MI/RTX showed an increased tendency in k10. RTX treatment had little effect on the metabolic profiles of the vagus. D. The MO also showed that k16 and k22 may be MI specific, while k23 is an intriguing profile solicited strongly by RTX, absent from MI/RTX, but a small subset of proteins share a similar profile in MI.

Figure 5. Treatment focused pathway enrichment heatmaps for proteins with long term expression changes. To focus on pathways that contained proteins with large fluctuations in expression over time, we selected proteins that had absolute delta-means ≥ 1.0 at 12-weeks and either/both of the 5 min and 24 h time points for each tissue/treatment group and again applied an enrichR analysis with the Reactome database. Pathways where the p-value > 0.01 are in grey and the heatmap is colored by $\log_2(2 + \text{enrichR-CombinedScore})$. Metabolism is a dominant pathway with differential protein expression in all treatments A) MI, B) MI/RTX, C) RTX. A Venn diagram including the three treatments was used to demonstrate the degree of overlap within these sets of Metabolism proteins (D).

Figure 1.

A

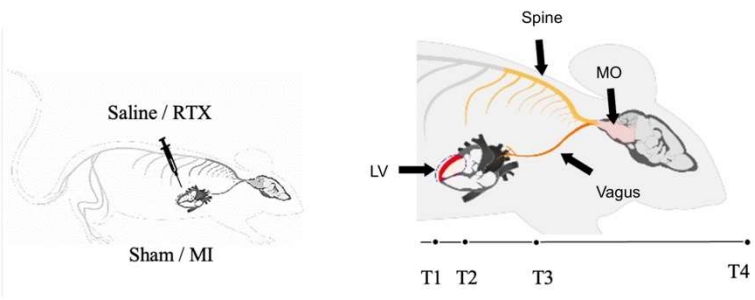
Saline / RTX
Sham / MI
Spine
MO
LV
Vagus
T1
T2
T3
T4

B

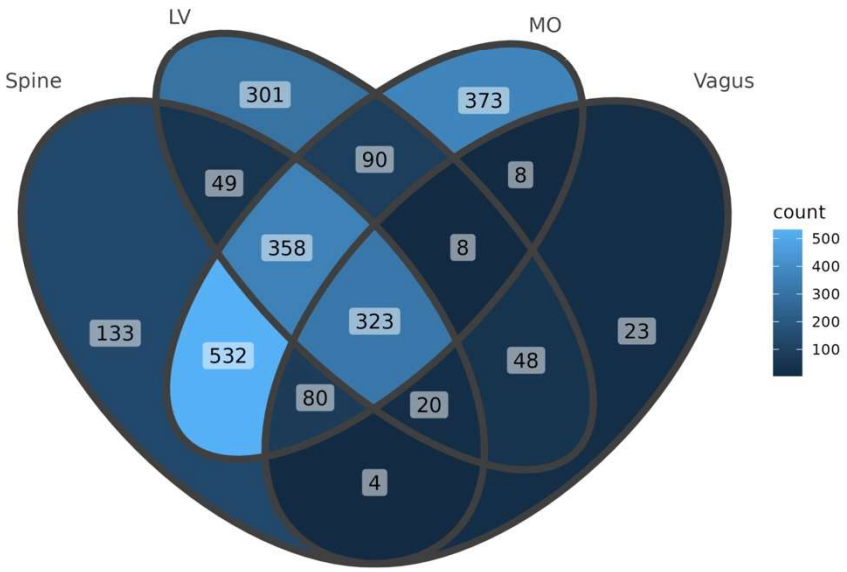
LV
MO
Spine
Vagus
301
373
49
90
8
358
8
133
532
323
23
48
80
20
4
count
500
400
300
200
100

Figure 2.

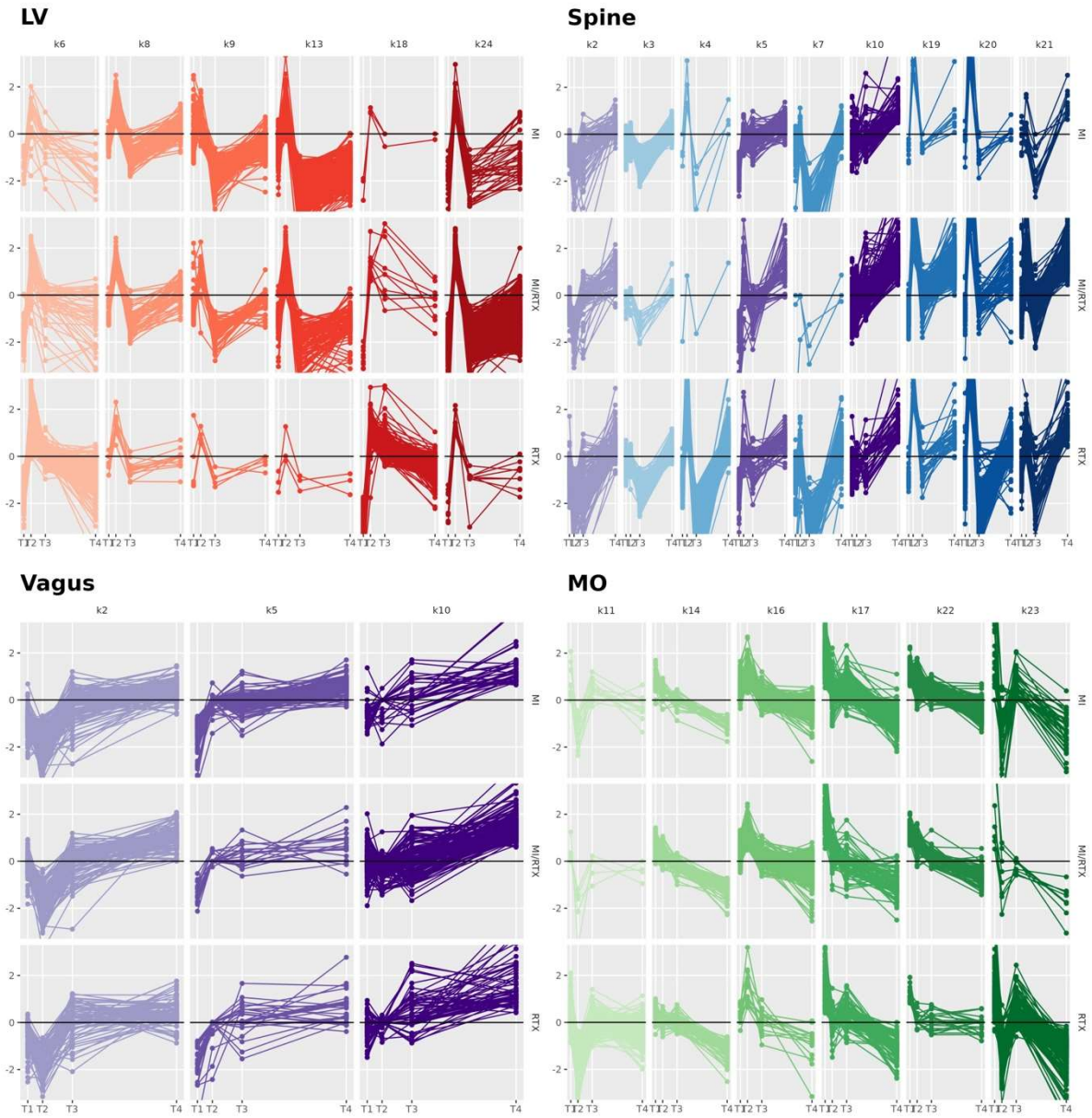
LV
k6
k8
k9
k13
k18
k24
Spine
k2
k3
k4
k5
k7
k10
k19
k20
k21
Vagus
k2
k5
k10
MO
k11
k14
k16
k17
k22
k23
MI
MI/RTX
RTX
T1 T2 T3 T4

Figure 3.

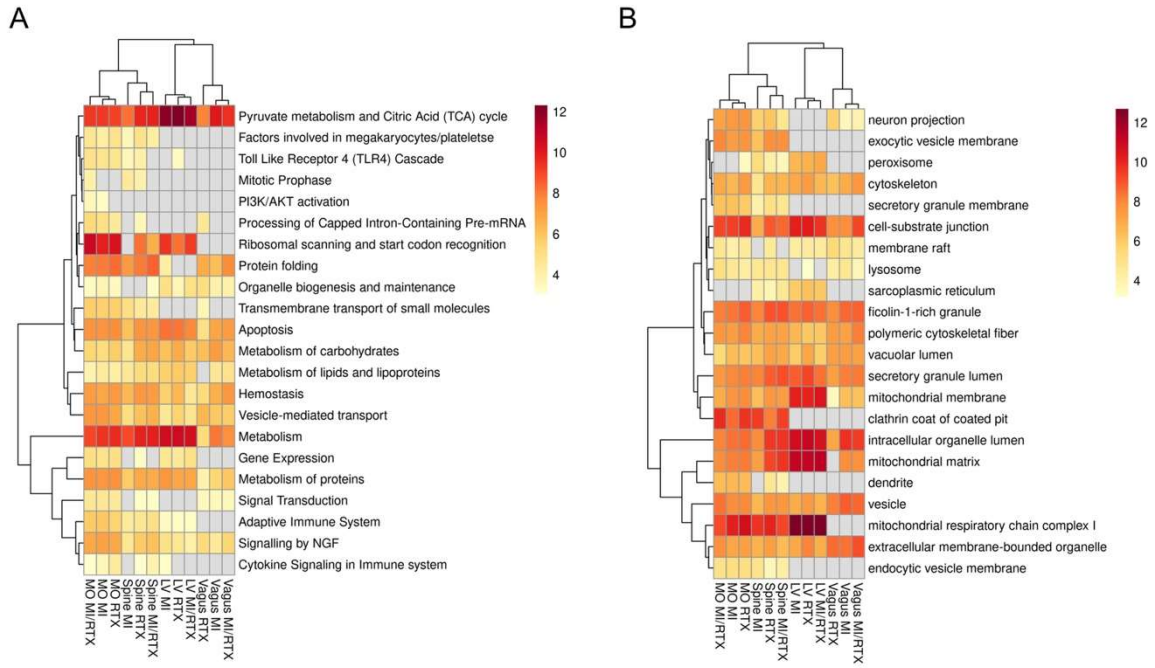
A
Pyruvate metabolism and Citric Acid (TCA) cycle
Factors involved in megakaryocytes/plateletse
Toll Like Receptor 4 (TLR4) Cascade
Mitotic Prophase
PI3K/AKT activation
Processing of Capped Intron-Containing Pre-mRNA
Ribosomal scanning and start codon recognition
Protein folding
Organelle biogenesis and maintenance
Transmembrane transport of small molecules
Apoptosis
Metabolism of carbohydrates
Metabolism of lipids and lipoproteins
Hemostasis
Vesicle-mediated transport
Metabolism
Gene Expression
Metabolism of proteins
Signal Transduction
Adaptive Immune System
Signalling by NGF
Cytokine Signaling in Immune system
12
10
8
6
4
MO MI/RTX
MO MI
MO RTX
Spine MI
Spine RTX
Spine MI/RTX
LV MI
LV RTX
LV MI/RTX
Vagus MI
Vagus RTX
Vagus MI/RTX
B
neuron projection
exocytic vesicle membrane
peroxisome
cytoskeleton
secretory granule membrane
cell-substrate junction
membrane raft
lysosome
sarcoplasmic reticulum
ficolin-1-rich granule
polymeric cytoskeletal fiber
vacuolar lumen
secretory granule lumen
mitochondrial membrane
clathrin coat of coated pit
intracellular organelle lumen
mitochondrial matrix
dendrite
vesicle
mitochondrial respiratory chain complex I
extracellular membrane-bounded organelle
endocytic vesicle membrane
12
10
8
6
4
MO MI/RTX
MO MI
MO RTX
Spine MI
Spine RTX
Spine MI/RTX
LV MI
LV RTX
LV MI/RTX
Vagus MI
Vagus RTX
Vagus MI/RTX

Figure 4.

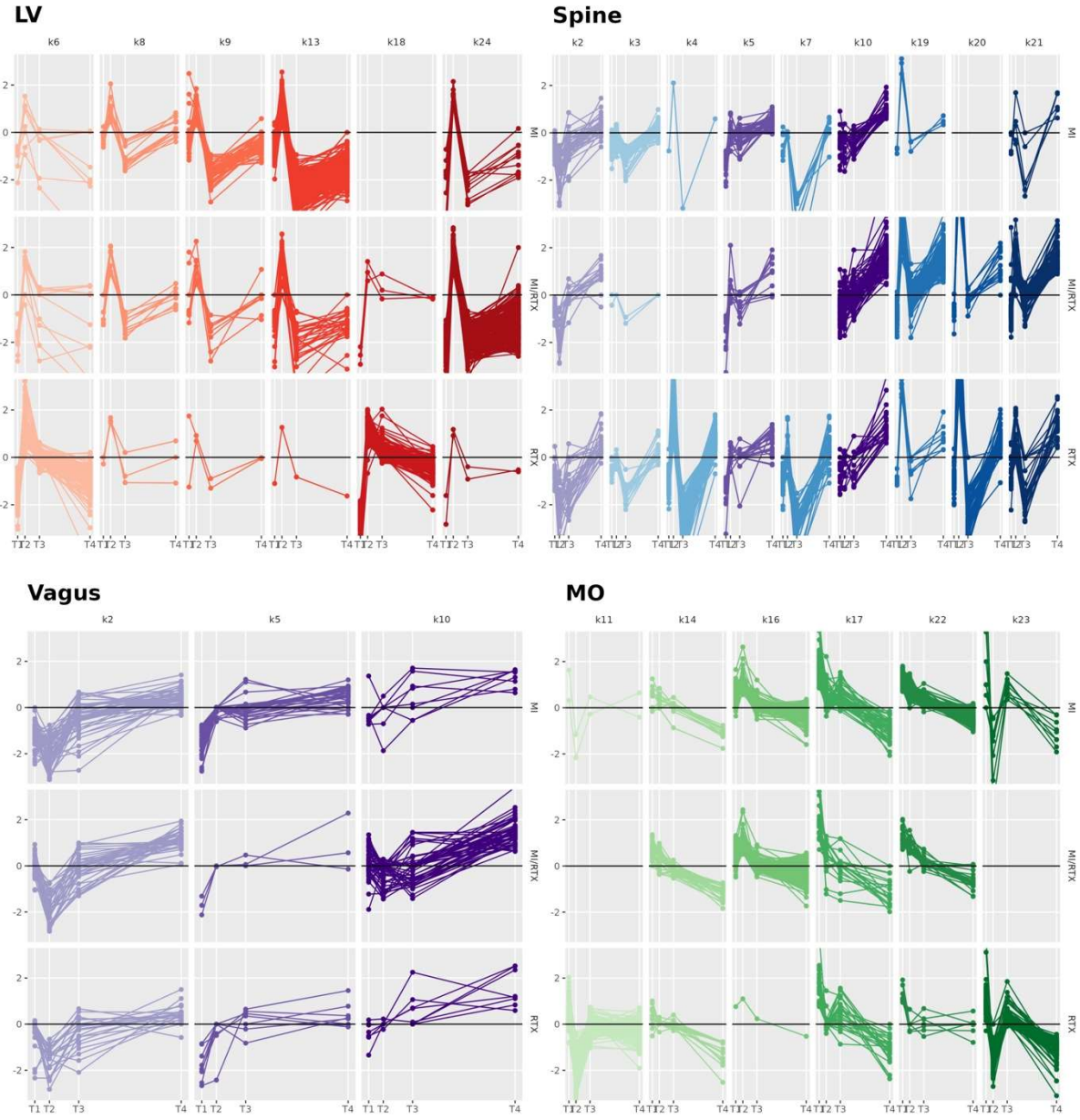
LV
k6
k8
k9
k13
k18
k24
Spine
k2
k3
k4
k5
k7
k10
k19
k20
k21
Vagus
k2
k5
k10
MO
k11
k14
k16
k17
k22
k23
MI
MI/RTX
RTX
T1 T2 T3 T4

Figure 5.

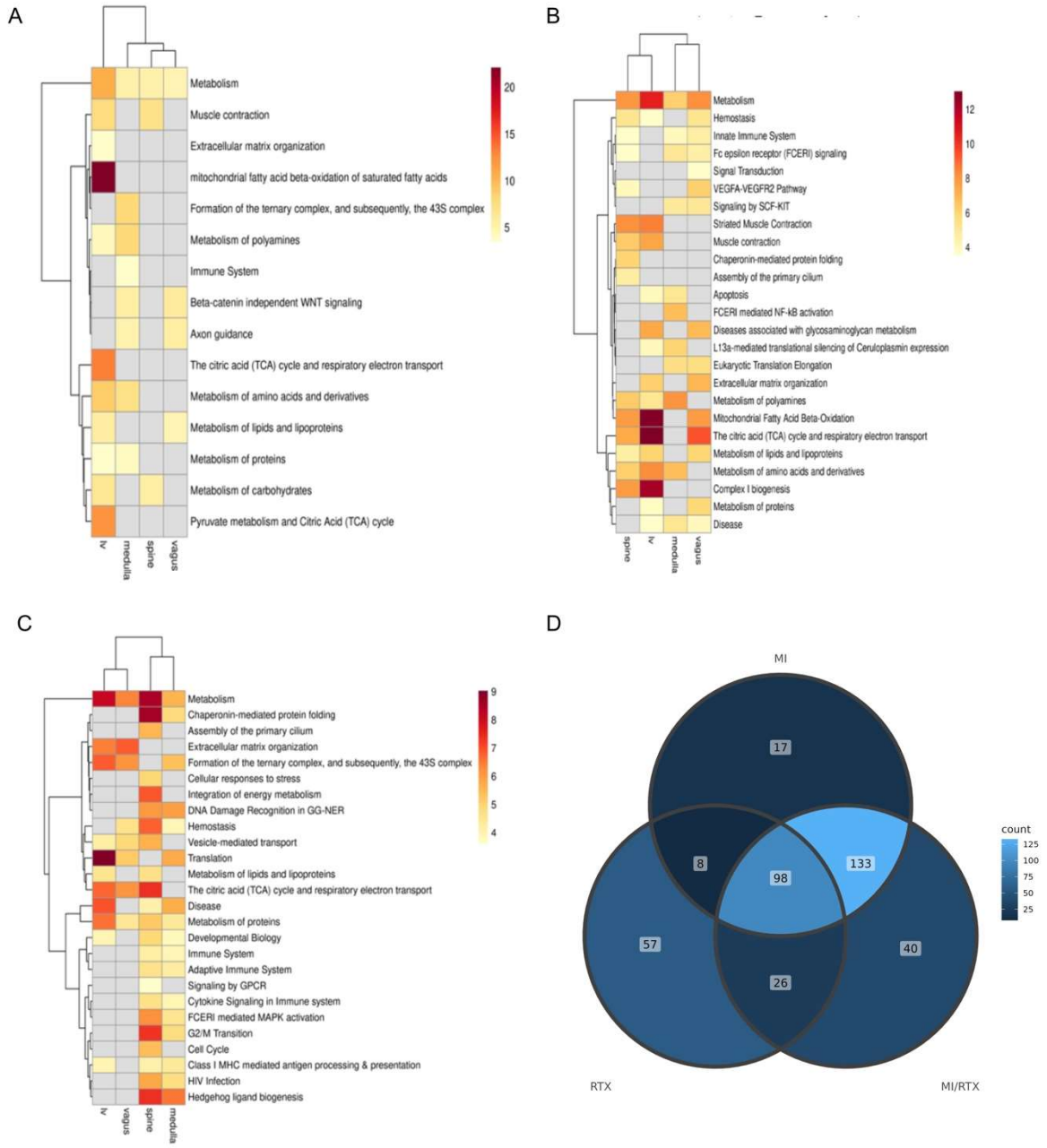
A
Metabolism
Muscle contraction
Extracellular matrix organization
mitochondrial fatty acid beta-oxidation of saturated fatty acids
Formation of the ternary complex, and subsequently, the 43S complex
Metabolism of polyamines
Immune System
Beta-catenin independent WNT signaling
Axon guidance
The citric acid (TCA) cycle and respiratory electron transport
Metabolism of amino acids and derivatives
Metabolism of lipids and lipoproteins
Metabolism of proteins
Metabolism of carbohydrates
Pyruvate metabolism and Citric Acid (TCA) cycle
20
15
10
5
IV
medulla
spine
vagus
B
Metabolism
Hemostasis
Innate Immune System
Fc epsilon receptor (FCERI) signaling
Signal Transduction
VEGFA-VEGFR2 Pathway
Signaling by SCF-KIT
Striated Muscle Contraction
Muscle contraction
Chaperonin-mediated protein folding
Assembly of the primary cilium
Apoptosis
FCERI mediated NF-kB activation
Diseases associated with glycosaminoglycan metabolism
L13a-mediated translational silencing of Ceruloplasmin expression
Eukaryotic Translation Elongation
Extracellular matrix organization
Metabolism of polyamines
Mitochondrial Fatty Acid Beta-Oxidation
The citric acid (TCA) cycle and respiratory electron transport
Metabolism of lipids and lipoproteins
Metabolism of amino acids and derivatives
Complex I biogenesis
Metabolism of proteins
Disease
12
10
8
6
4
spine
IV
medulla
vagus
C
Metabolism
Chaperonin-mediated protein folding
Assembly of the primary cilium
Extracellular matrix organization
Formation of the ternary complex, and subsequently, the 43S complex
Cellular responses to stress
Integration of energy metabolism
DNA Damage Recognition in GG-NER
Hemostasis
Vesicle-mediated transport
Translation
Metabolism of lipids and lipoproteins
The citric acid (TCA) cycle and respiratory electron transport
Disease
Metabolism of proteins
Developmental Biology
Immune System
Adaptive Immune System
Signaling by GPCR
Cytokine Signaling in Immune system
FCERI mediated MAPK activation
G2/M Transition
Cell Cycle
Class I MHC mediated antigen processing & presentation
HIV Infection
Hedgehog ligand biogenesis
9
8
7
6
5
4
IV
vagus
spine
medulla
D
MI
17
8
98
133
57
40
26
RTX
MI/RTX
count
125
100
75
50
25